ORIGINAL ARTICLE

Selective Laser Melted Porous Ti-6Al-4 V Scaffolds: Modelling, Manufacturing, and Effect of Microstructure on Mechanical Properties

**Palash Mondal[1] · Adil Wazeer[2] · Apurba Das[3] ·
Amit Roy Chowdhury[4] · Amit Karmakar[1]**

Abstract Ti-6Al-4 V alloy is widely used in medical implants, particularly in orthopedics application. Additive manufacturing (AM), specifically selective laser melting (SLM) is useful for porous scaffolds fabrication where complex passages facilitaes bone re-growth. This study focused on the modeling, manufacture, and testing of microstructure and mechanical characteristics of seven different scaffolds (Diamond, Cross, Grid, Vinties, Tesseract, Star, and Octet) of 15 mm cube with 65% porosity. Average pore area and strut thickness of scaffolds are measured using Stereo microscope. All these fabricated scaffolds are experimentally tested under compressive loads in INSTRON testing machine. The compressive test results are also compared with the numerical simulation results generated using finite element analysis (ANSYS) software. Maximum load cell capacity of ± 25 kNis used during compression testing in INSTRON. The Grid type scaffold shows maximum ultimate compressive strength of 101.39 MPa and an effective elastic moduli of 10.33 GPa with an average pore area of 2,417,618.517 μm^2 and strut thickness of 740.249 μm. This variant of the scaffold will be more compatible with the human bone's elasticity, and it can also mitigate stress-shielding effects during healing.

1 Introduction

Titanium alloys are commonly used as metallic implants in orthopedic applications due to their superior elastic modulus, corrosion resistance, specific stiffness, and excellent biocompatibility [1]. However, the Ti-6Al-4 V alloy has a significantly higher elastic modulus than human bone [2], leading to potential adverse effects on the scaffold-bone interface and bone resorption [3]. Novel Ti alloy scaffolds with excellent bone-compatibility , elastic moduli [4] and porous designs aim to mitigate stress shielding. Currently, Stainless Steel (316L) is extensively used for various implants, while Co-Cr alloys are commonly used in orthodontics, knee replacements, and hip prostheses [5]. The focus is on creating implants that facilitate bone growth within scaffolds, enhancing healing and fixation motives [6].

The solid Ti alloys have a higher elastic modulus (E = 110 GPa) compared to bone tissues (E = 10 – 12 GPa), leading to uneven load distribution, implant loosening, and bone fractures [7]. Stress shielding exacerbates this issue at the junction between hard tissues and conventional metallic implants. The incorporation of a porous structure mitigates this by aligning the effective elastic modulus with the patient's specific bone characteristics [8]. Porous scaffolds play a crucial role in preventing osteonecrosis and promoting bone tissue development, adhesion, and proliferation [9]. The microstructure of the bone graft

✉ Apurba Das
 adiiestme@gmail.com

1 Department of Mechanical Engineering, Jadavpur University, Kolkata 700032, India

2 School of Materials Engineering, Purdue University, West Lafayette, IN 47907, USA

3 Mechanical Engineering Department, Indian Institute of Engineering Science and Technology-Shibpur, Howrah 711103, India

4 Aerospace Engineering and Applied Mechanics Department, Indian Institute of Engineering Science and Technology-Shibpur, Howrah 711103, India

must be osteoconductive for proper osseointegration in the implant [10]. Optimal pore size is critical for cell development in regenerative applications, with reported ranges of 50–500 μm for load-bearing bone grafting and pores larger than 300 μm promoting vascularization [11]. However, achieving an optimal size appears to be highly dependent on specific applications. In the SLM process, metal powder is melted layer by layer using concentrated laser scanning or electron beams. The internal structure and geometry are precisely controlled by adjusting laser power based on a CAD model. Argon gas prevents oxidation in the SLM. Heat treatments are necessary to enhance the ductility of SLM components [12].

Irregular pore surfaces and strut corrugation create local heterogeneities, intensifying stress concentrations. Heinl et al. used the selective electron beam melting (SEBM) technique to produce porous Ti-6Al-4 V, demonstrating that mechanical properties such as stiffness, yield stress, and ultimate compressive stress follow a linear trend on a logarithmic scale [13]. Parthasarathy et al. highlighted the significant impact of strut size on the mechanical characteristics of porous Ti-6Al-4 V alloy components produced using SEBM [14]. Cheng et al. reported that variations in cooling rate affect the microstructure and mechanical properties of porous Ti-6Al-4 V [15].

AM technique is now a widely research topic for implant production where layered materials are printed to get custom-specific implants using SLM process. Rhino 6 CAD software is used to design 3D porous scaffold models then it is saved as STL file format, which converts the 3D models into number of 2D slices for AM processing. Parthasarathy et al. [16] and Jardini et al. [17] have used AM to create porous implants, especially for Ti-6Al-4 V alloy in biomedical applications [18–20]. Despite limited literature on the design and characterization of Ti-6Al-4 V scaffolds, AM holds significant promise in bone tissue engineering for personalized orthopedic surgeries. This study details the modeling, manufacturing, and mechanical testing of seven porous scaffolds with 65% porosity using SLM, comparing theoretical and actual porosity and subjecting the samples to compressive loads.

2 Material Selection and Methods

2.1 Powder Material

Ti-6Al-4 V powders of smooth surface and a particle diameter of 80 μm, are used to fabricate porous scaffolds. Figure 1(a) shows the morphological image, emphasizing the nearly spherical geometry, while Fig. 1(b) shows the particle size distribution determined through the Coulter principle and laser diffraction. The powder monolayer is visually examined using an optical microscope GX51 from EOS, Finland.

The scaffolds are made according to the chemical configuration presented in Table 1, and it is observed that percentages of Fe, C, H, O & N in Ti-6Al-4 V powder are quite minimal.

(a)   (b)
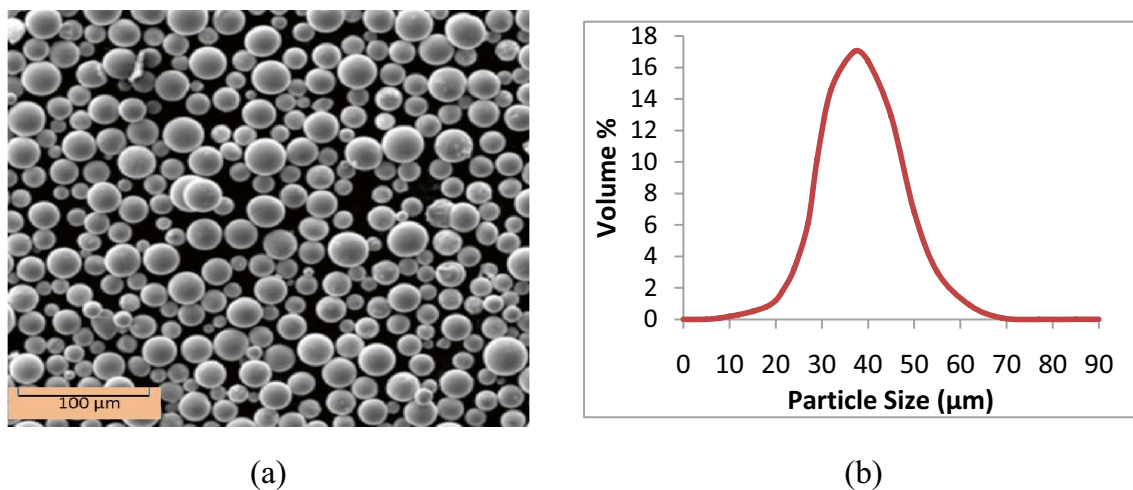
Fig. 1 **a** Ti-6Al-4 V raw powder's morphological image for SLM Manufacturing; **b** Ti-6Al-4 V powder's particle size distribution

Table 1 - Ti-6Al-4 V powders used in the study have the following chemical composition

Element	Ti (wt%)	Al (wt%)	V (wt%)	Fe (ppm)	C (ppm)	H(ppm)	O(ppm)	N(ppm)
Mass	Balance	5.5 -6.75	3.5—4.5	< 3000	< 800	< 150	< 2000	< 500

Laser power, scanning speed, hatch spacing, and layer thickness are the main four process parameters that influence SLM technology. Porosity has significant effects upon mechanical properties and the density of parts. The energy density is calculated as [21]:

$$E_d = \frac{P_l}{(v_s h t)} \tag{1}$$

where E_d = energy density, P_l = laser power, v_s = scan speed, h = hatch distancing and t = layer thickness. Input process factors, such as layer thickness, scanning speed, and hatch distance, influence energy density. Higher energy promotes increased melting but diminishes with greater layer thickness, scanning speed, and hatch distance. The process parameters governs the energy input for SLM process, which may be defined as [22]:

$$E_i = \frac{4P_l}{(\pi d_l^2 v_s)} \tag{2}$$

where E_i = energy input, P_l = laser power, d_l = diameter of laser beam and v_s = scan speed.

Linear energy density (LED) is employed for determining the energy input of powder materials as [23]:

$$LED = \frac{P_l}{v_s} \tag{3}$$

where P_l = laser power and v_s = scan speed.

The correlation between the porosity % (P) and the input process parameters- energy density (E_d), laser power (P_l), scanning speed (v), and hatch distancing (h) may be written as:

$$P = f(\frac{E_d v_s h^2}{p_l}) \tag{4}$$

The scanning speed (v_s), hatch distancing (h) and layer thickness (t) are all directly proportionate to building rate. The scanning speed and layer thickness are controlled by the existing laser power. Product of scanning speed, hatch distancing, and layer thickness determines the rate of building of the SLM procedure, which may be defined as:

$$V_b = v_s h t \tag{5}$$

where V_b = the building rate (mm³/s).

2.2 Design and Fabrication of Porous Ti-6Al-4 V Scaffolds

Rhino 6 software is used for designing seven distinct types (each of two, n = 14 scaffolds) of 3D porous scaffolds such as Diamond, Grid, Cross, Vinties, Tesseract, Star, and Octet of Ti-6Al-4 V alloy of 15 mm cubes (ISO: 13,314:2011) having 65% porosity and fabricated by SLM technique as shown in Fig. 2. For Ti-6Al-4 V porous scaffolds, a specific density of 4.41 g/cm³ and a relative density of 99.8% are used.

The scaffolds are heat treated for 120 min at 900°C at a rate of 50°C/min before being cooled to ambient temperature in a furnace having inert (argon) atmosphere. Inside the construction chamber, oxygen level is controlled below 8 ppm.

## 2.3 Selective Laser Melting (SLM) Process for Ti-6Al-4 V

SLM, a metal AM technique introduced in 2002 for the production of complex part. Figures 3, 4 depict a typical SLM machine and its procedure. A blade deposits a layer of metallic powder onto the build platform, and the laser melts the powder into 2D cross sections in an inert environment. The galvanometer controls beam focus, and the F-theta lens guides beam movement. The building platform lowers for each layer (15–150 µm thickness) until the 3D part is completed. Initially the 3D models are designed in Rhino 6 and then saved as STL files, converting to 2D layers through slicing algorithm. AM has diverse biomedical applications, including tissue and organoid formation, body implants, anatomical models, and personalized prostheses. Figure 5 illustrates computer layouts and actual samples on the machine bed.

2.4 Morphological Characterization

The Selective Laser Melting (SLM) fabricated porous Ti-6Al-4 V scaffolds accurately replicated the specified design structures. However, the fabricated porous scaffolds exhibited dimensional disparities in both strut thickness and pore size, ranging between 2–6%. These differences are primarily due to shrinkage during solidification and the attachment of Ti powders to the scaffold walls during fabrication. Variations can also result from the system's capabilities, such as the minimum spot size of the laser beam [24] and powder properties [25]. It was observed that the actual pore size was larger and the strut size thinner compared to the designed structures. Additionally, struts were found to have micropores, mainly in the lower portions of the porous samples, likely due to unsintered particles causing uneven melting. The average pore area and strut thickness of all the scaffolds are measured by stereo microscope (Model—Stemi 508) and are shown in Fig. 6.

2.5 Experimental Setup

Compression tests on an INSTRON machine are conducted to determine the mechanical properties of each sample. An additional attachment (shown in Fig. 7) with two 5 mm thick
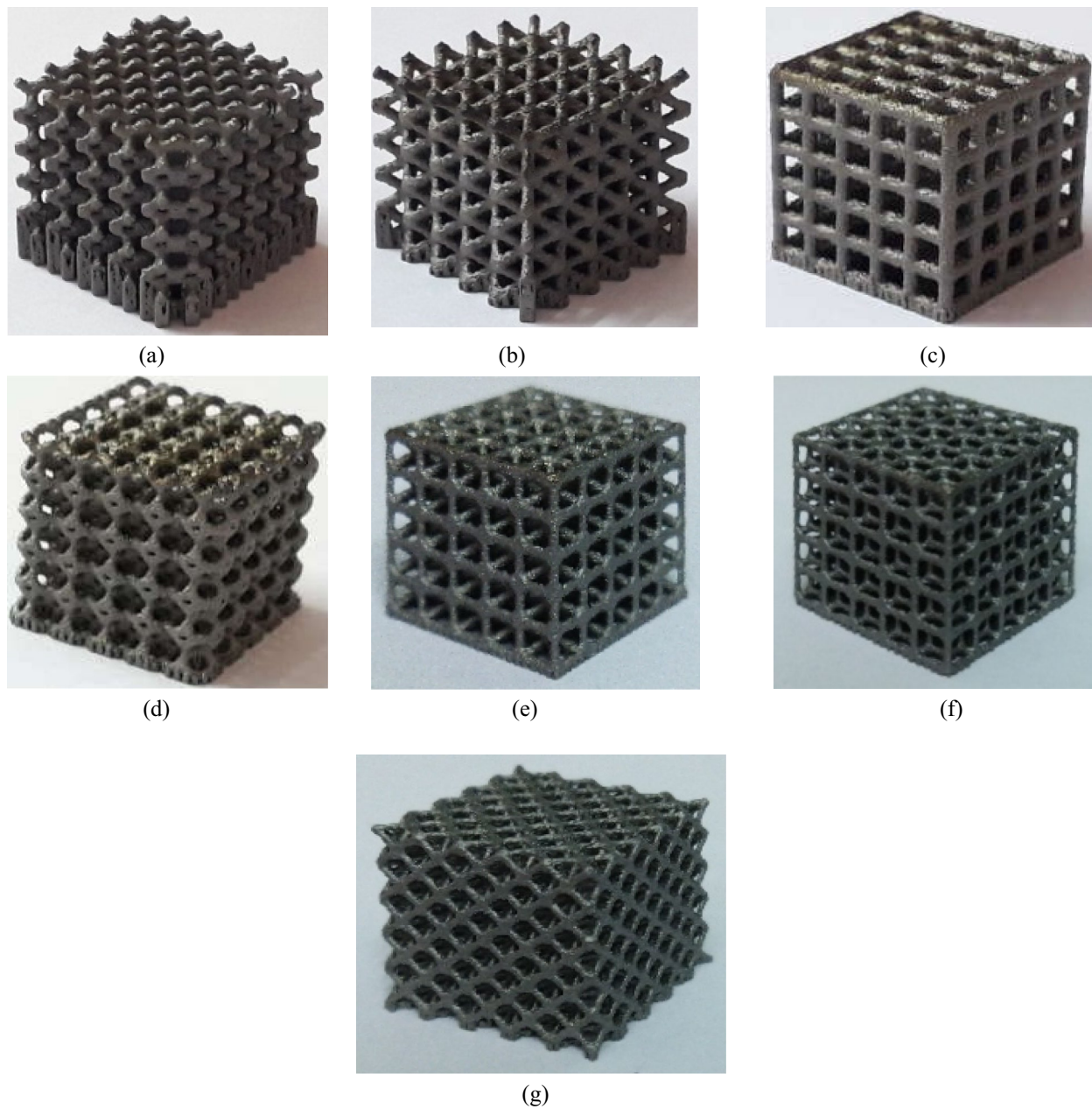
Fig. 2 Fabricated Ti64 Porous Scaffolds by SLM: **a** Diamond, **b** Cross, **c** Grid, **d** Vinties, (e) Tesseract, **f** Star, and **g** Octet

high-speed steel compression platen is created to ensure proper fitting and prevent slippage during the compression test of small-sized samples (15 mm cube). The attachment, connected to the INSTRON machine, stabilized the sample and reduced compression effects.

3 Results and Discussion

3.1 Effect and Optimisation of Process Parameters During SLM Process
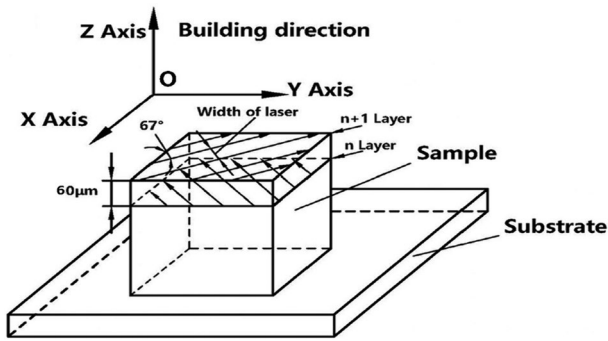
The laser power, scanning speed, layer thickness, and

Fig. 3 SLM Manufacturing Process

hatch distancing are the primary input process parameters that affect the microstructure of porous scaffolds in SLM process. All seven scaffolds are fabricated using a SLM machine (Model- EOSINT M280-400W), and the input process parameters for Ti-6Al-4 V materials given in Table 2.

The main objective of fabricating SLM porous scaffolds is to achieve dense, solid struts with a specified total porosity, aiming to enhance rigidity. It's crucial to verify accuracy through distinct microstructure observation. Rapid cooling of the melted pool during operation can lead to anomalies in desired mechanical properties.

Fig. 8 illustrates the impact of process parameters (laser power, hatch distance, and scan speed) on the relative density of Ti-6Al-4V samples produced by SLM, highlighting the significant influence of scanning speed. Optimized process parameters are listed in Table 3 to achieve required strut density. Additionally, powder layer thickness influences the surface roughness and microstructure of porous scaffolds.

The correlation between volume energy density (VED) and relative density can be made from Equation No. 1. Figure 8 illustrates that as VED increases, relative density initially rises and the decreses, reaching a maximum near 100% at 40 J/mm³. Figure 9 shows increased porosity with higher scanning speed and hatch distance, except for laser power (Eq. 4). An optimal ratio of laser power to scan speed (0.272 J-mm) and hatch distance (0.12 mm) enhances relative density, preventing issues like spheroidization or incomplete melting.
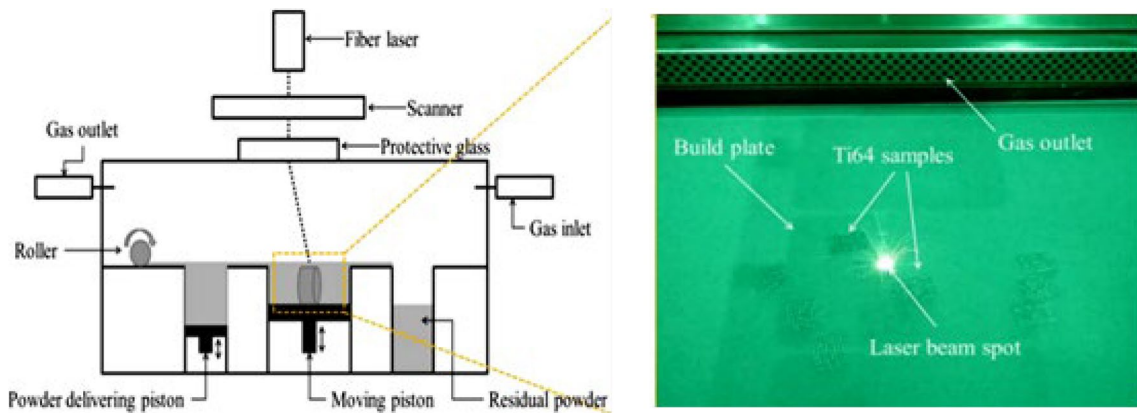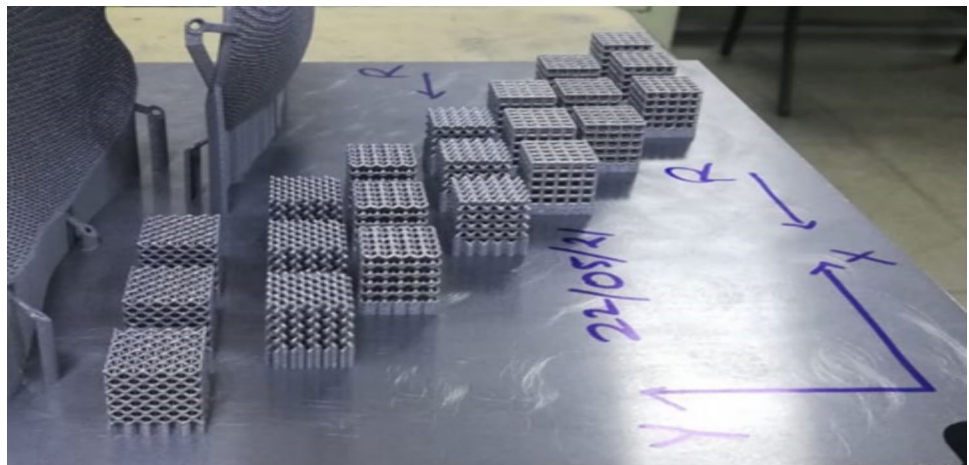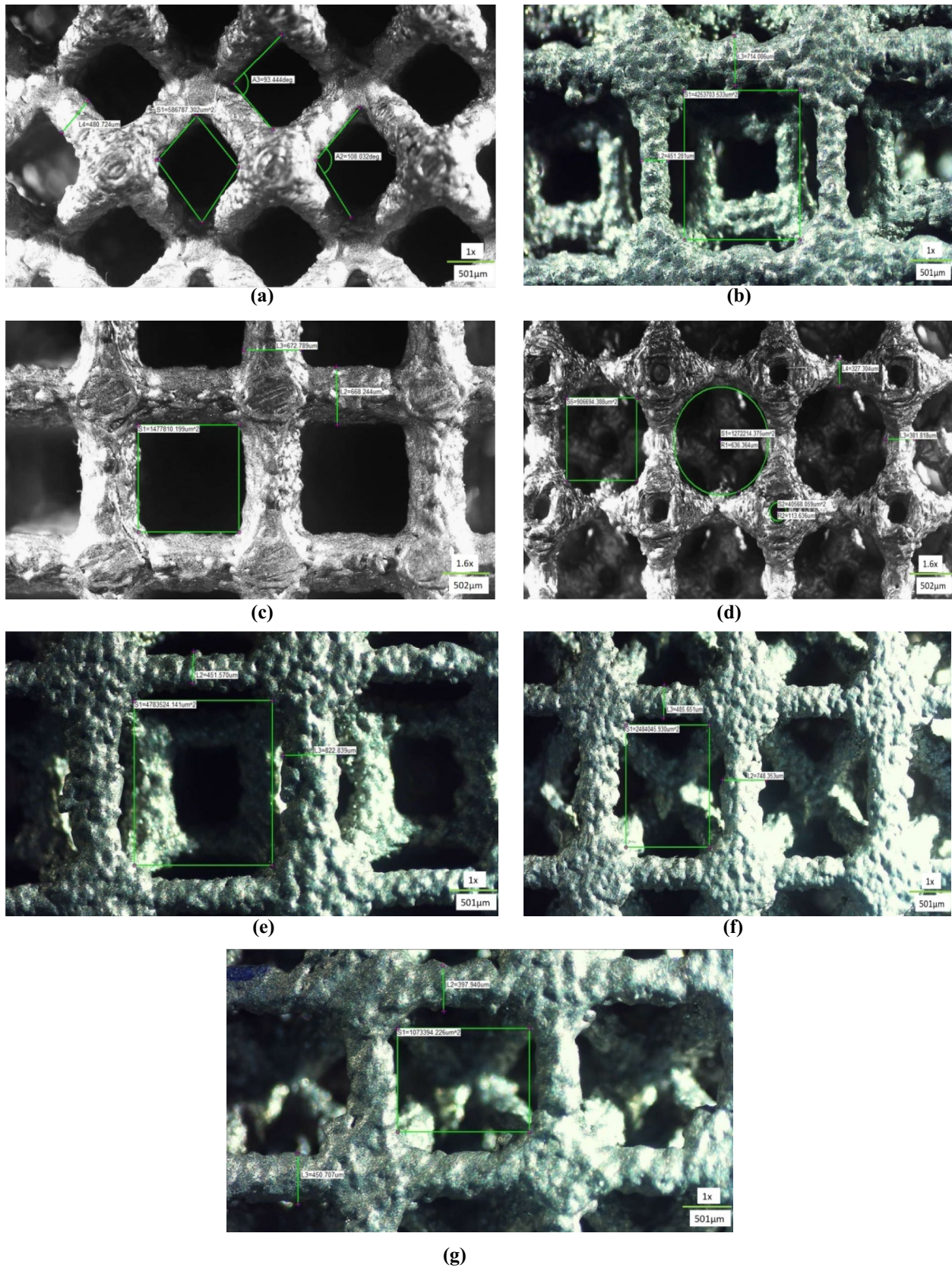

Fig. 4 Schematic of a typical Selective Laser Melting (SLM) procedure used to create Ti-6Al-4 V porous structures using EOSINT-M280
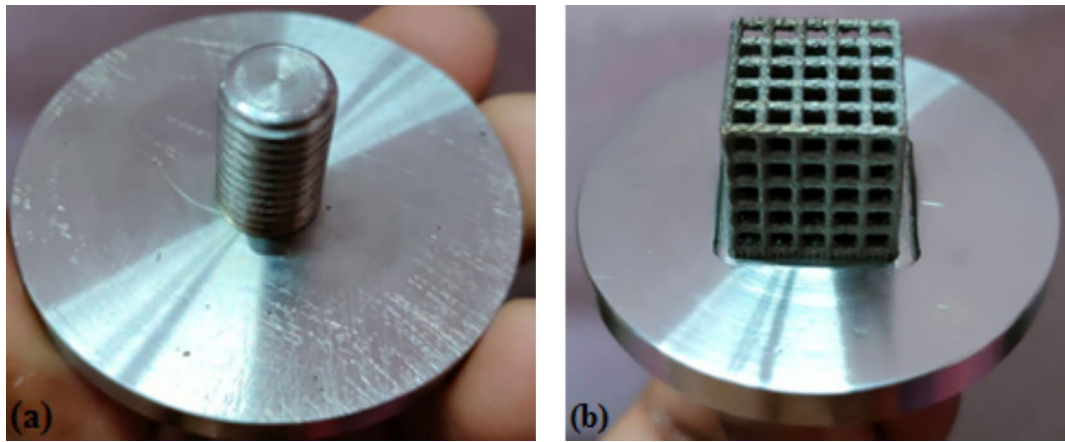
Fig. 5 Manufactured scaffolds on printing board

Fig. 6 Measurement of pore area and strut thickness using stereo microscope (Stemi 508) of fabricated porous scaffolds: **a** Diamond, **b** Cross, **c** Grid, **d** Vinties, **e** Tesseract, **f** Star, **g** Octet

Fig. 7 HSS plates to be fitted with INSTRON machine: **a** Upper plate and **b** Lower plate
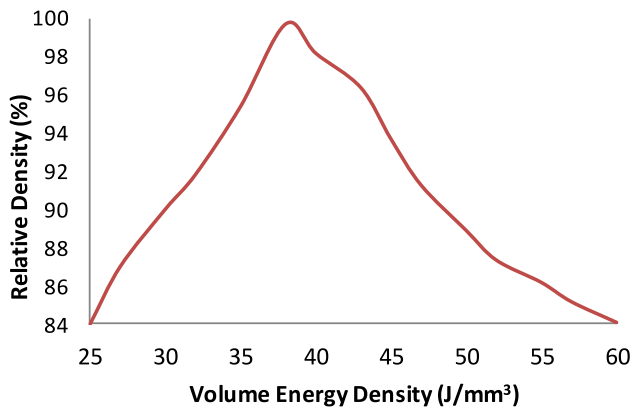
Table 2 – Input process parameters used for Ti64 alloy during fabrication by SLM

Parameters	Value
Laser Type	Ytterbium Fibre Laser
Spot Shape	Spherical
Scan Speed (SS)	800–1500 mm/s
Particle Diameter (PD)	80 μm
Hatch Distance (HD)	0.1- 0.14 mm
Laser Power (LP)	
Laser Diameter (LD)	217- 400 W
80 micron	
Density (ρ)	4.41 g/cm^3
Layer Thickness (LT)	60 μm
Initial Bed Temp. (T$_i$)	35^0 C
Scan Angle of Rotation	67^0
Building Space	200 mm×200 mm×200 mm
Environment Maintained	Inert

Table 3 - Optimized process parameters and build system of Ti-6Al-4 V using SLM

Parameters	Result
Scan Speed (SS)	1250 mm/s
Laser Power (LP)	340 W
Hatch Distance (HD)	0.12 mm
Layer Thickness (LT)	0.06 mm

Figure 9 illustrates varied densification with hatch spacing (95 μm to 140 μm) for different scan speed and laser power. Optimal densification (up to 99.5%) is achieved with a higher hatch spacing (120 μm), lower laser power (22 W), and slower speed (1150 mm/s), allowing sufficient heat buildup. Alternatively, a higher power (340 W) and speed (1250 mm/s) with 120 μm hatch spacing achieve proper density and faster construction. Simulation models provide insights into optimal processing parameters, eliminating the need for extensive testing.

3.2 Measurement of Surface Roughness (R$_a$)

The implant and bone tissue may be affected by surface roughness of implants, which can also inhibit osteoblastic cell adhesion, growth, proliferation, and differentiation. Surface roughness has a positive effect on implants if R$_a$ is less than 25 μm and a negative effect if R$_a$ is larger than 57 μm. Porous implants do not require surface treatment up to a roughness value of 25 μm. Surface roughness (Ra) is measured using a Talysurf tester (MITUTOYO SJ-210) and reported in Table 4.

The grid sample exhibits lower surface roughness, while the diamond type shows the highest roughness. Specifically, the grid sample has a roughness value of less than 25 μm, eliminating the need for additional surface treatment.

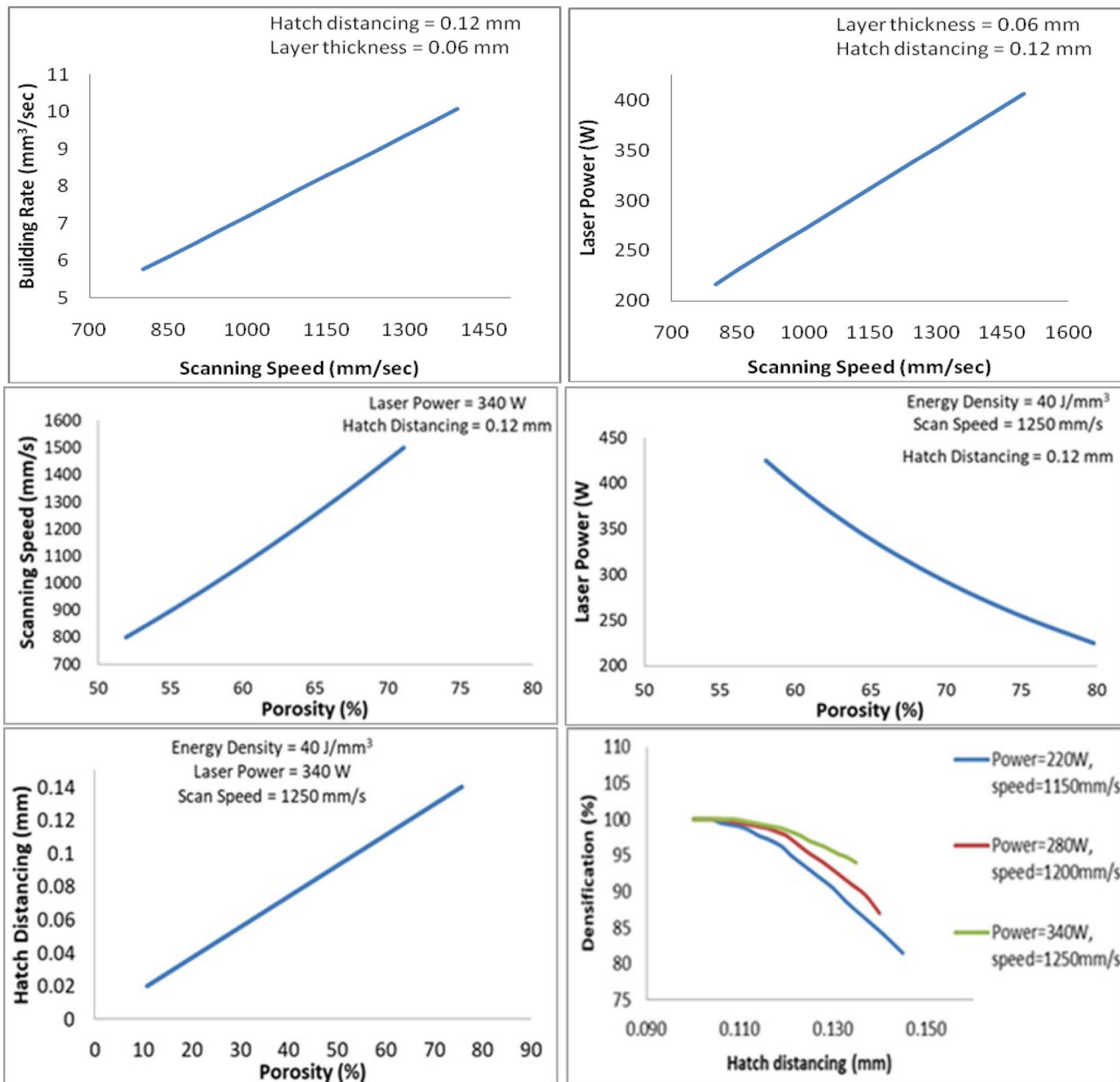**Fig. 8** Variation in relative density (%) with volume energy density (J/mm^3)

Fig. 9 Effect of input process parameters during fabrication by SLM

Table 4 – Average roughness (R_a) of different fabricated samples

Sample Type	Average roughness (R_a) in µm	
	Sample-1	Sample-2
Diamond	46.2	49.6
Cross	43.7	41.8
Grid	23.2	21.6
Vinties	27.7	29.8
Tesseract	31.3	30.6
Star	33.8	35.1
Octet	29.3	31.6

3.3 Measurement of Porosity

The actual porosity values for each sample are evaluated using Archimedes principle (shown in Fig. 10) and presented in Table 5. The actual porosity percentage of Ti-6Al-4V scaffolds can be determined as:

$$P = (1 - \frac{W_p}{W_d})x100\% \tag{6}$$

where, P = Porosity, W_p = Weight of the porous sample and W_d = Weight of the densed samples.

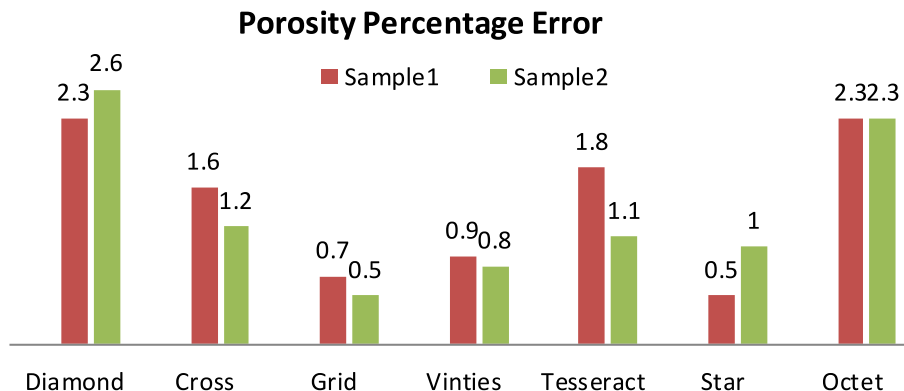**Fig. 10** Measuring cylinders being used to measure the porosity of the fabricated porous scaffolds

Table 5 - Measured porosity of fabricated scaffolds

Sample Type	Theoretical porosity	Measured porosity	
		Sample 1	Sample 2
Diamond	65%	62.7%	62.4%
Cross	65%	63.4%	63.8%
Grid	65%	64.2%	64.5%
Vinties	65%	64.4%	64.6%
Tesseract	65%	63.2%	63.9%
Star	65%	64.5%	64.0%
Octet	65%	62.7%	62.7%

The actual porosity percentage of fabricated scaffolds decreases by an average of 1–4% compared to the designed porosity, attributed to metal powders adhering to the scaffold walls during fabrication. The grid-type sample exhibits the lowest percentage of inaccuracy, whereas the diamond-type sample shows the highest difference in porosity (shown in Fig. 11).

3.4 Mechanical Properties

The theoretical mechanical properties of Ti-6Al-4 V alloys manufactured through the SLM technique are evaluated following ASTM E8 standards.

The relationship between modulus of elasticity and porosity % can be written as [26]:

$$E_p = E_s(1 - P)^2 \tag{7}$$

where E_p = effective elastic modulus of porous material, E_s = elastic modulus of solid material and P = porosity. The Gibson-Ashby Correlation model [27] is employed to assess the relationship between porosity and elastic properties in the fabricated scaffolds. The relationship between elastic modulus, strength and porosity can be written as:

$$E_p/E_s = C_1(W_p/W_s)a \tag{8}$$

$$\sigma_p/\sigma_s = C_2(W_p/W_s)b \tag{9}$$

where, E_p = elastic modulus of porous scaffolds, E_s = elastic modulus of Ti alloy,

Fig. 11 Error in porosity percentage of different fabricated scaffolds

Porosity Percentage Error

W_p = weight of porous scaffolds, W_s = weight of Ti alloy, σ_p = strength of of Ti alloy, σ_s = strength of of Ti alloy, a, b, C_1 and C_2 are constants. Consider E_s = 110 GPa [28] and σ_s = 1050 MPa [29].

Using Eq. (1), Eqs. (2) and (3) can be re-written as:

$$E_p/E_s = C_1(1 - P)a \qquad (10)$$

$$\sigma_p/\sigma_s = C_2(1 - P)b \qquad (11)$$

where, a = 2, b = 1.5, C_1 = 1 and C_2 = 0.3 is used as per Gibson-Ashby model [30].

With increasing porosity %, effective elastic modulus decrease (shown in Fig. 12). The theoretical effective elastic modulus may be determined using Eq. (7) and is equal to 13.475 GPa (assuming a porosity of 65% and a elastic modulus of 110 GPa), similar to human bones (E = 3 – 30 GPa).

As porosity increases, both the relative compressive strength and relative elastic modulus of scaffolds decrease, as illustrated in Figs. 13, 14.

3.5 Compression test

An aniaxial compressive testing is performed on the scaffolds using the INSTRON machine, recording load variations and deformation behaviors. The stress–strain curve and compressive elastic moduli are obtained from the test results presented in Table 6. The compressive stress–strain curves of the scaffolds is shown in Fig. 15. Pore area and strut thickness of the tested scaffolds are shown in Fig. 16 using the same stereo microscope.

Dense Ti alloys have a higher elastic modulus (110 GPa) compared to human bones (E = 3—30 GPa). In the SLM method, Ti-6Al-4 V materials have stronger strength and stiffness, but poorer ductility (E = 110 GPa, yield strength = 945 MPa, UTS = 1050 MPa, and strain % = 14%) [31]. The effective elastic modulii of scaffolds are measured by the slope of stress–strain curves obtained from compression test on an INSTRON machine. For grid type sample,
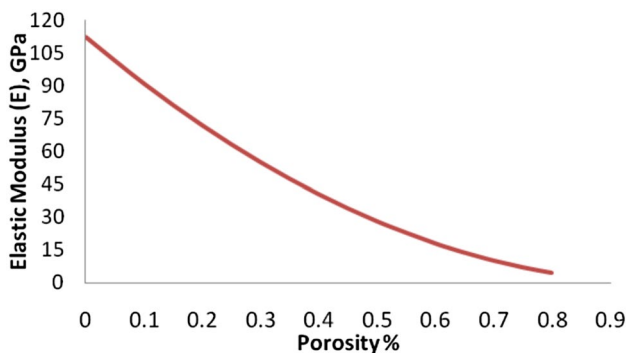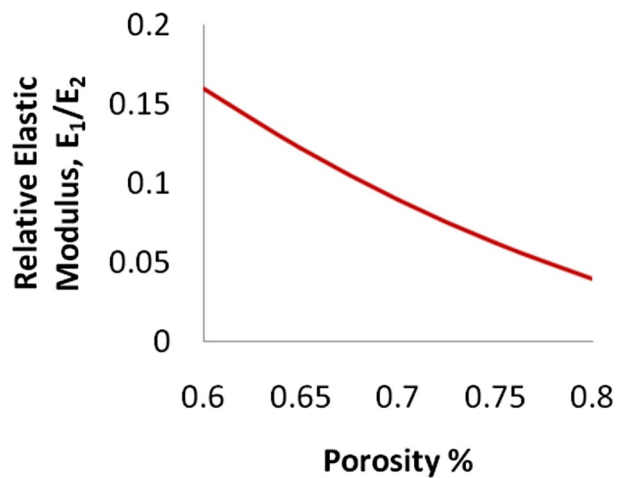

Fig. 13 Relative elastic modulus, E_1/E_2 vs Porosity %

the greatest value of compressive strength (101.39 MPa) and average elastic modulus (10.33 GPa) is observed. The results show that the grid samples are slightly hard at first due to their form, but when additional load is applied, they become soft and strain increases.

Tesseract, star and octet scaffolds don't meet the biomedical needs as metallic implants in case of compressive load of 25 kN and above as they are fractured. As opposed to that, diamond, cross, grid and vinties scaffolds remain unchanged even after compressive loading of 25 kN due to their higher average strut thickness as compared with tesseract, star and octet types and to reach the fracture point for these scaffolds additional load is required. A larger collapse in load is observed with a larger strut thickness. The stress is found to increase linearly up to the limit of proportionality, after which, its slope decreases. At this point, bending is seen in the strut. Further increase in load caused the strut to break
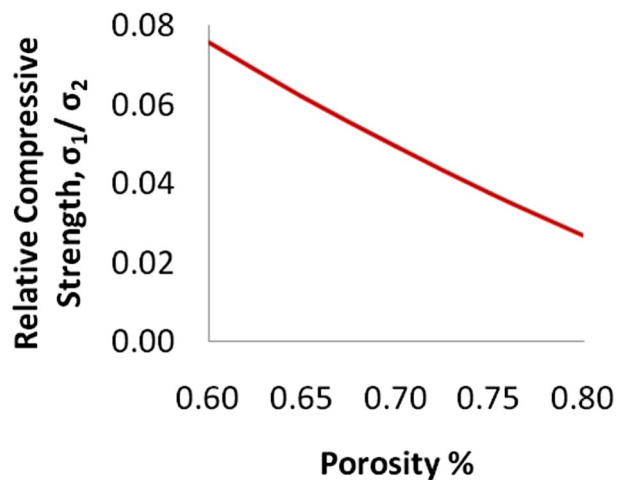

Fig. 12 The effect of porosity on elastic modulus

Fig. 14 Relative compressive strength, σ_1/σ_2 vs Porosity %

Table 6 - A comparison of mechanical properties between Ti-6Al-4 V scaffolds by SLM and natural bones

Scaffolds Type	Actual Porosity %	Pore Size (μm²)	Strut Thickness (μm)	UCS (MPa)	E (GPa)
Diamond	*62.55*	*586,787.302*	*496.929*	96.41	6.5
Cross	*63.6*	*4,253,703.533*	*601.184*	98.42	11.15
Grid	*64.4*	*2,417,618.517*	*740.249*	101.39	10.33
Vinties	*64.14*	*1,290,453.750*	*485.438*	95.63	7.16
Tesseract	*63.55*	*4,783,524.141*	*451.570*	94.92	5.87
Star	*62.45*	*2,484,045.93*	*407.651*	92.71	7.9
Octet	*62.7*	*1,175,303.449*	*467.599*	96.49	11.16
Natural bones	*–*	*–*	*–*	0.45—25.8	3—30
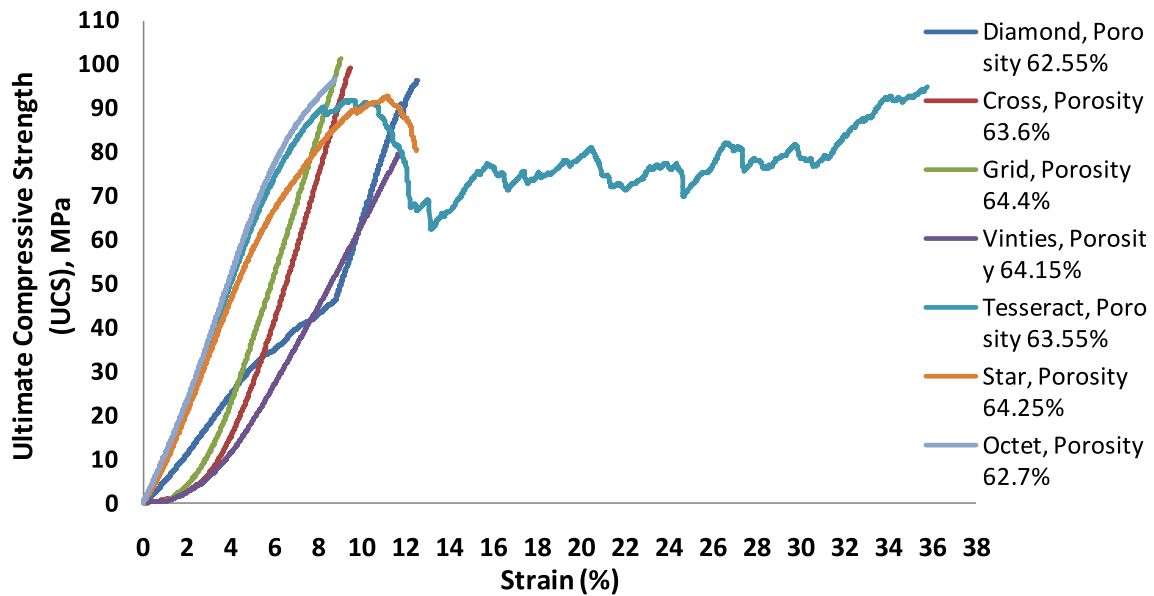
Fig. 15 Compressive stress–strain curve of porous Ti-6Al-4 V scaffolds obtained from INSTRON

with a snap noise. From Table 6, it is observed that UCS increases with increase in strut size and the maximum UCS is found as 101.39 MPa for grid type scaffold with highest strut thickness of 740.249 μm. The microstructure of all the seven tested scaffolds at same compressive load is shown in Fig. 16.

The manufactured scaffolds have a promising elastic modulus that is colser to natural cortical bones (E = 3—30 GPa). Table 6 reveals that it has a greater compressive strength than bone (compressive strength ranges from 0.45 to 25.8 MPa). The stress-shielding effect is reduced as the similar elastic modulus of scaffolds and human bones. On the other hand, the implant's lifespan is extended as the compressive strength of fabricated scaffolds is higher than that of human bones.

3.6 Finite Element Simulation

ANSYS (2020 R2) software is used for finite element analysis (FEA). A 25 kN compressive force is applied uniformly over the upper surface of the porous scaffolds whereas the lower surface is fixed. Then the experimental results validated the FE analysis, as shown in Fig. 17. For the diamond, cross, grid, vinties, tesseract, star, and octet, the maximum Von-Mises stresses and strain percentage of modeled scaffolds shows 95.07 MPa, 96.90 MPa, 100.21 MPa, 92.99 MPa, 88.86 MPa, 83.38 MPa & 84.15 MPa, and 12.07%, 13.00%, 8.28%, 9.15%, 8.8%, 9.19% and 10.35% respectively. For each kind of scaffold, the results of the compressive test and the finite element analysis are closely matching.
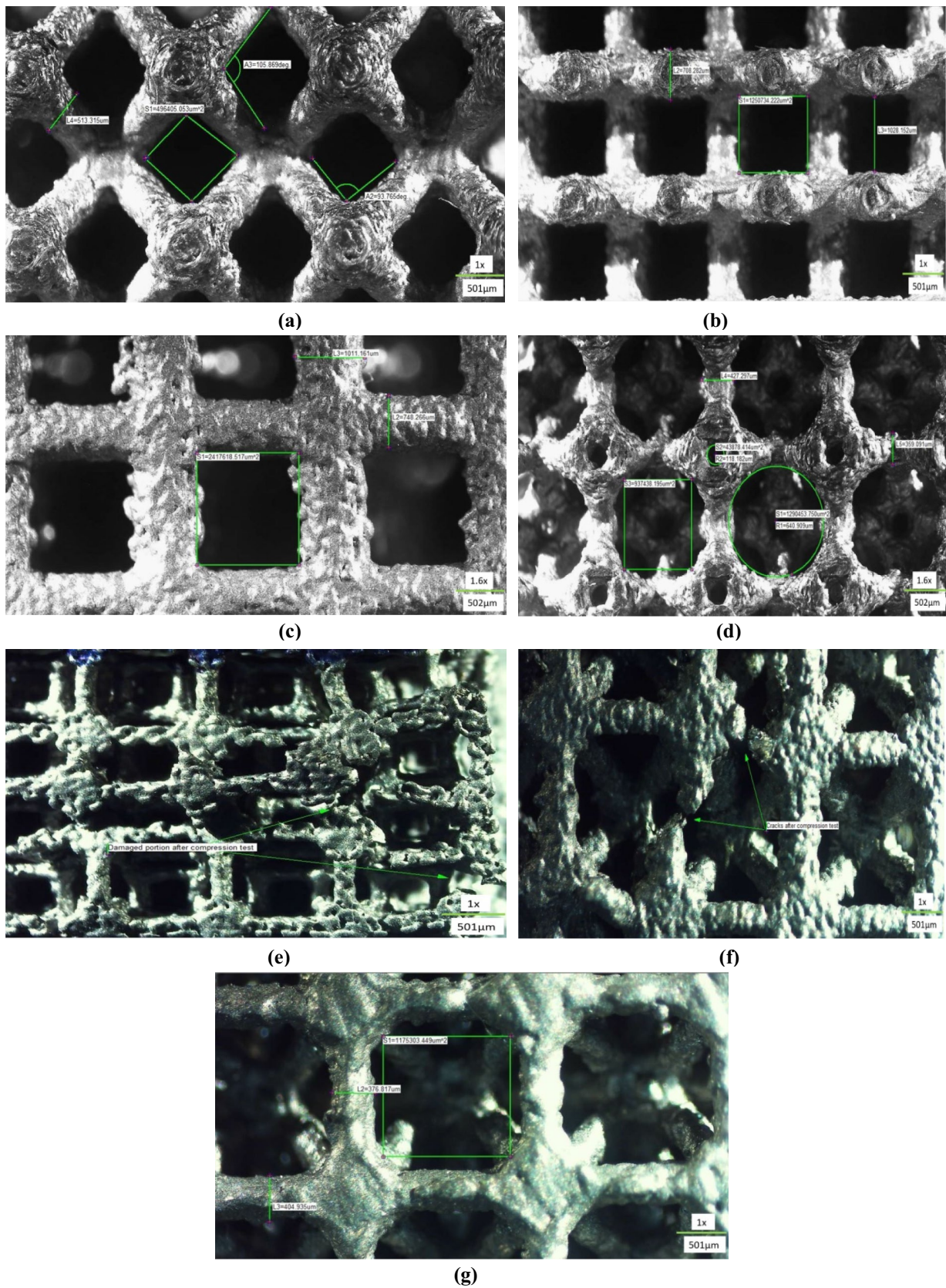
Fig. 16 Measurement of pore area and strut thickness using stereo microscope (Stemi 508) of the tested scaffolds: **a** Diamond, **b** Cross, **c** Grid, **d** Vinties, **e** Tesseract, **f** Star & **g** Octet
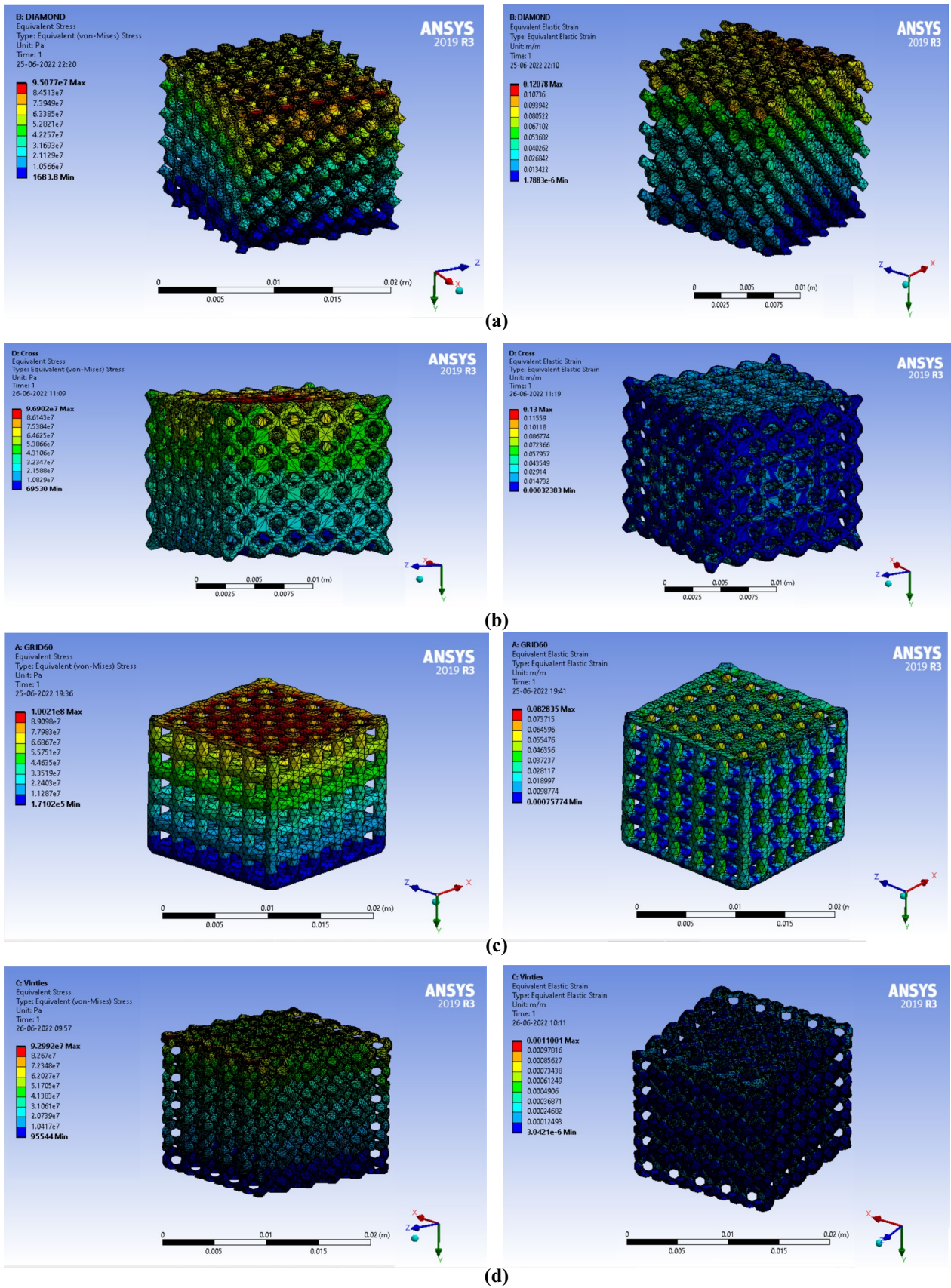
Fig. 17 Finite element analysis of designed porous scaffolds by ANSYS: **a** Diamond, **b** Cross, **c** Grid, **d** Vinties, **e** Tesseract, **f** Star & **g** Octet
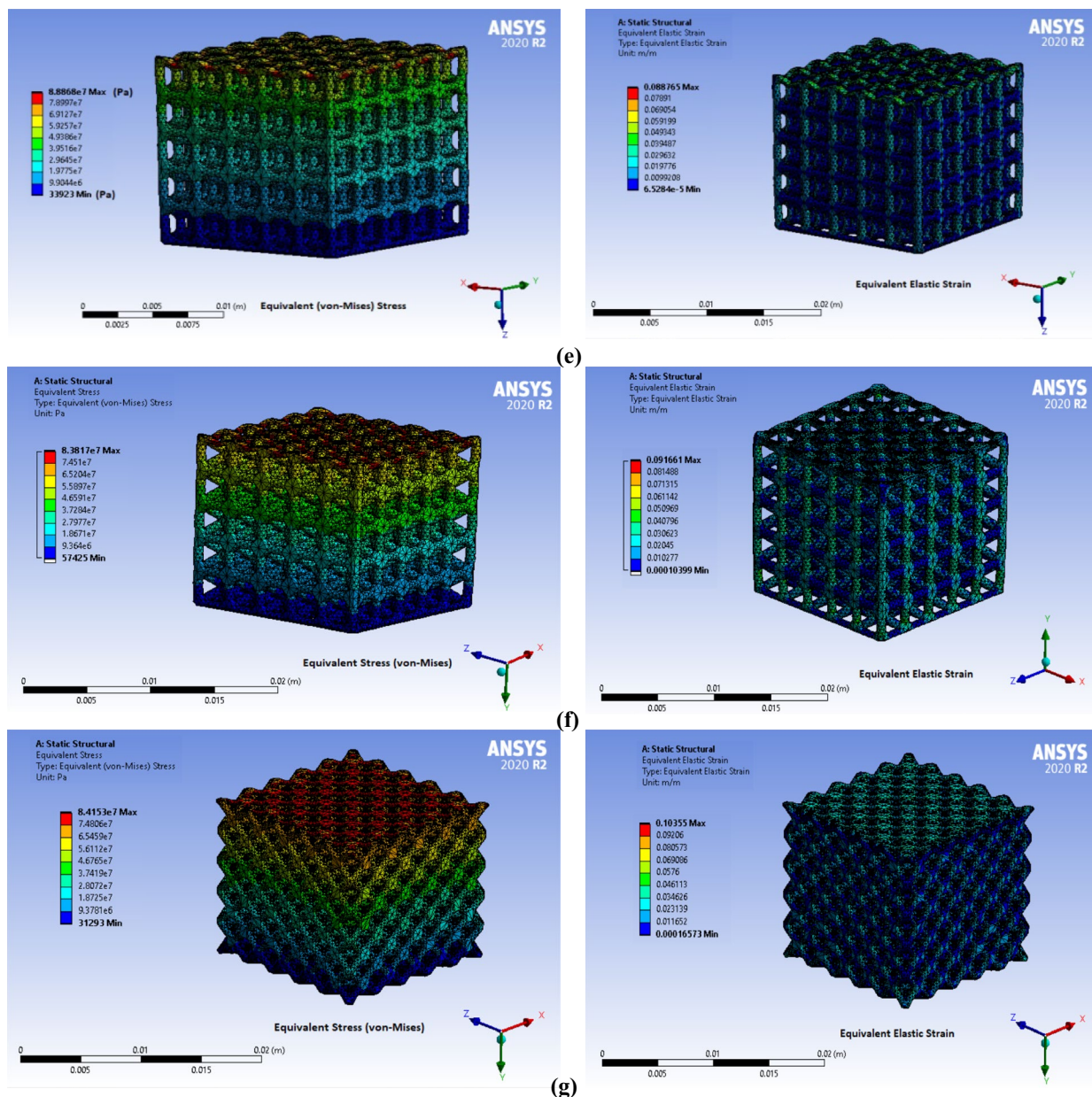
(e)

(f)

(g)

Fig. 17 (continued)

4 Conclusion

Based on the current work, the following conclusions can be listed:

1. The grid type sample has the lowest error in porosity %, whereas the diamond type has the highest, and the grid type sample may produce better likeness with the lowest deviation.
2. The grid type sample has the least amount of surface roughness, but the diamond type sample has the greater value of surface roughness.

3. Porosity % increases with increase in energy density, scanning speed, hatch distancing but decreases with laser power.
4. By optimising the process parameters, the microstructure of porous Ti64 alloy scaffolds may be controlled during SLM, which are: 340 W laser power, 1250 mm/s scanning speed, 0.12 mm hatch spacing and 0.06 mm powder layer thickness.
5. When volume energy density (VED) is 40 J/mm^3, the relative density reaches its highest value, which is close to 100%.

6. The porosity % of scaffolds affects the mechanical properties. The effective elastic modulus, relative density and relative compressive strength decrease as the porosity % increases.

7. The elastic modulus of Ti alloy scaffolds with 65% porosity is similar to human bones, which will reduce the effect of stress-shielding.

8. The ultimate compressive strength (UCS) of scaffolds is much more than human bones results improving the implant's longevity. The grid type scaffold shows maximum UCS (101.39 MPa) as its strut thickness (740.249 μm) is more.

9. Ti alloys can be successfully linked in biomedical sectors due to additive manufacturing technologies, which have the capacity to construct any complicated porous scaffold for biomedical applications.

References

1. Liu X, Chu P K, and Ding C, Surface modification of titanium, titanium alloys, and related materials for biomedical applications. *Materials Science and Engineering: R: Reports.* **47** (3–4), (2004) 49–121.

2. Long M, and Rack H J, Titanium alloys in total joint replacement- a materials science perspective. *Biomaterials.* **19** (18), (1998) 1621–1639.

3. Niinomi M, Recent research and development in titanium alloys for biomedical applications and healthcare goods. *Science and technology of advanced Materials.* **4** (5), (2003) 445.

4. Niinomi M, Mechanical biocompatibilities of titanium alloys for biomedical applications. *Journal of the mechanical behavior of biomedical materials.* **1** (1), (2008) 30–42.

5. Bordjih K, Jouzeau J Y, Mainard D, et al., Evaluation of the effect of three surface treatments on the biocompatibility of 316L stainless steel using human differentiated cells. *Biomaterials.* **17** (5), (1996) 491500

6. Bandyopadhyay A, Espana F, Balla V K, et al., Influence of porosity on mechanical properties and in vivo response of Ti6Al4V implants. *Acta biomaterialia.* **6** (4), (2010) 1640–1648.

7. Carnelli D, Lucchini R, Ponzoni M, et al., Nanoindentation testing and finite element simulations of cortical bone allowing for anisotropic elastic and inelastic mechanical response. *Journal of biomechanics.* **44** (10), (2011) 1852–1858.

8. Limmahakhun S, Oloyede A, Sitthiseripratip K, et al., Stiffness and strength tailoring of cobalt chromium graded cellular structures for stress-shielding reduction. *Materials & Design.* **15** (114), (2017) 63341.

9. Chen Z, Yan X, Yin S, et al., Influence of the pore size and porosity of selective laser melted Ti6Al4V ELI porous scaffold on cell proliferation, osteogenesis and bone ingrowth. *Materials Science and Engineering: C.* **1** (106), (2020) 110289

10. Albrektsson T A, and Johansson C J, Osteoinduction, osteoconduction and osseointegration. *European Spine Journal* **10** (2001) S96–S101.

11. Karageorgiou V, and Kaplan D, Porosity of 3D biomaterial scaffolds and osteogenesis. *Biomaterials* **26** (27), (2005) 5474–5491.

12. Vrancken B, Thijs L, Kruth J P, et al., Heat treatment of Ti-6Al-4V produced by Selective Laser Melting: Microstructure and mechanical properties. *Journal of Alloys and Compounds.* **15** (541), (2012) 177–185.

13. Heinl P, Körner C, and Singer R F, Selective electron beam melting of cellular titanium: mechanical properties. *Advanced Engineering Materials.* **10** (9), (2008) 882–888.

14. Parthasarathy J, Starly B, and Raman S, A design for the additive manufacture of functionally graded porous structures with tailored mechanical properties for biomedical applications. *J Manuf Process* **13** (2011) 160–170.

15. Cheng X Y, Li S J, Murr L E, et al., Compression deformation behavior of Ti–6Al–4V alloy with cellular structures fabricated by electron beam melting. *Journal of the mechanical behavior of biomedical materials.* **1** (16), (2012) 153–162.

16. Parthasarathy J, 3D modeling, custom implants and its future perspectives in craniofacial surgery. *Annals of maxillofacial surgery.* **4** (1), (2014) 9.

17. Jardini A L, Larosa M A, de CarvalhoZavaglia C A, et al., Customised titanium implant fabricated in additive manufacturing for craniomaxillofacial surgery: This paper discusses the design and fabrication of a metallic implant for the reconstruction of a large cranial defect. *Virtual and physical prototyping.* **9** (2), (2014) 115–125.

18. Mondal P, Das A, Karmakar A, et al., Biomedical porous scaffold fabrication using additive manufacturing technique: Porosity, surface roughness and process parameters optimization. *International Journal of Lightweight Materials and Manufacture* **5** (3), (2022) 384–396.

19. Mondal P, Das A, Karmakar A, et al. Effect of Heat Treatment on Compressive Behavior of Selectively Laser Melted Ti64 Scaffolds. Journal of The Institution of Engineers (India): Series D (2022): 1–9.

20. Mondal P, Das A, Karmakar A, et al. Fabrication of Ti-6Al-4V Porous Scaffolds Using Selective Laser Melting (SLM) and Mechanical Compression Test for Biomedical Applications. Journal of The Institution of Engineers (India): Series D (2022): 1–10.

21. Vandenbroucke B, and Kruth J P, Selective laser melting of biocompatible metals for rapid manufacturing of medical parts. *Rapid Prototyping Journal* **13** (2007) 196–203.

22. Liu Y, Yang Y, Mai S, et al., Song, Investigation into spatter behavior during selective laser melting of AISI 316L stainless steel powder. *Materials & Design* **87** (2015) 797–806.

23. H. Attar, M. Bermingham, S. Ehtemam-Haghighi, et al. Evaluation of the mechanical and wear properties of titanium produced by three different additive manufacturing methods for biomedical application, Materials Science & Engineering: A (2019).

24. Metel A S, Stebulyanin M M, Fedorov S V, et al., Power density distribution for laser additive manufacturing (SLM): potential, fundamentals and advanced applications. *Technologies.* **7** (1), (2018) 5.

25. Farzadi A, Waran V, Solati-Hashjin M, et al., Effect of layer printing delay on mechanical properties and dimensional accuracy of 3D printed porous prototypes in bone tissue engineering. *Ceramics International.* **41** (7), (2015) 8320–8330.

26. Su XB, YANG YQ, Peng YU, et al. Development of porous medical implant scaffolds via laser additive manufacturing. Transactions of Nonferrous Metals Society of China. 2012 Oct 1;22:s181–7.

27. Ashby MF, Gibson LJ. Cellular solids structure and properties; Press Synd. Univ. Cambridge: Cambridge, UK. 1997:175–231.

28. Vilaro T, Colin C, and Bartout J D, As-fabricated and heat-treated microstructures of the Ti-6Al-4V alloy processed by selective laser melting. *Metallurgical and materials transactions A.* **42** (10), (2011) 3190–3199.

29. Liu S, and Shin Y C, Additive manufacturing of Ti-6Al-4V alloy: A review. *Materials & Design.* **15** (164), (2019) 107552

30. Trevisan F, Calignano F, Aversa A, et al., Additive manufacturing of titanium alloys in the biomedical field: processes, properties and applications. *Journal of applied biomaterials & functional materials.* **16** (2), (2018) 57–67.

31. Frosch K H, Barvencik F, Lohmann C H, et al., Migration, Matrix Production and Lamellar Bone Formation of Human Osteoblast-Like Cells in Porous Titanium Implants. *Cells Tissues Organs* **170** (4), (2002) 214–227.